



Aptamer-immobilized bone-targeting nanoparticles in situ reduce sclerostin for osteoporosis treatment



Yuting Niu^{a,c,1}, Yang Yang^{a,c,1}, Zhen Yang^{a,c}, Xu Wang^{a,c}, Ping Zhang^{a,c}, Longwei Lv^{a,c}, Yan Liu^{b,c,*}, Yunsong Liu^{a,c,*}, Yongsheng Zhou^{a,c,*}

^a Department of Prosthodontics, Peking University School and Hospital of Stomatology

^b Laboratory of Biomimetic Nanomaterials, Department of Orthodontics, Peking University School and Hospital of Stomatology

^c National Center of Stomatology & National Clinical Research Center for Oral Diseases & National Engineering Research Center of Oral Biomaterials and Digital Medical Devices & Beijing Key Laboratory of Digital Stomatology & Research Center of Engineering and Technology for Computerized Dentistry Ministry of Health

ARTICLE INFO

Article history:

Received 9 February 2022

Received in revised form 14 April 2022

Accepted 9 June 2022

Available online xxxx

Keywords:

Nanoparticle

Aptamer

Osteoporosis treatment

Bone-targeting

Sclerostin

ABSTRACT

Bone-targeted drug delivery to reduce systemic complications and maintain sufficient doses in bone tissues is the main challenge for osteoporosis treatment. Here, we develop a novel, and simply synthesized bone-targeting nanomedicine (DNA-MSN, DNAM) containing a PEGylated dendritic mesoporous silica nanoparticle (MSN) core (~ 65 nm) and an anti-sclerostin aptamer (Aptscl56) layer, to treat osteoporosis. The nanoparticle core protects the immobilized Aptscl56 from rapid nuclease degradation and renal filtration, prolonging *in vivo* half-lives. The DNAM-immobilized Aptscl56 layer exhibits dual functions to direct bone-attachment of ovariectomized mice, due to the interaction between phosphate groups in DNA aptamer Aptscl56 and bone calcium in hydroxyapatites, and to *in situ* capture sclerostin with picomolar affinities. Moreover, we show DNAM significantly reverses the serum level of sclerostin and osteoporotic bone loss to a normal level, improving bone histomorphology parameters and mechanical properties in the femur, and recovering serum levels of bone turnover markers, without systemic toxicity. Notably, the therapeutic effect of DNAM is superior to the "gold standard" drug alendronate, and the systemic dose of DNAM-immobilized Aptscl56 is only 25% of free Aptscl56. The present study provides insights into the regulation of unwanted circulating biohazards and represents a promising approach to deliver nanomedicines to treat osteoporosis.

© 2022 Elsevier Ltd. All rights reserved.

Introduction

Osteoporosis is one of the most common musculoskeletal diseases, destroying bone microstructures, reducing bone strength and bone mass, and increasing the risks of fractures, severe complications and even death [1,2]. Bones, compared to other organs like livers, spleens or kidneys [3], are less vascularized for drug penetration. The off-target drug absorption and the systemic administration of conventional drugs in a large dose/long term result in increased systemic toxicity and reduced therapeutic effects [4]. For example, estrogen supplement leads to some non-skeletal side effects, such as breast carcinoma and vascular events [5]. Long-term

administration of bisphosphonates (BPs), such as alendronate (ALN) [6], the most commonly used drug for osteoporosis, can cause severe osteonecrosis of the jaw [7,8]. Even more, prolonged use of parathyroid hormones, such as teriparatide, increases the risk of bone cancers [9]. Therefore, it is a major challenge to improve bone-targeted delivery of drugs and to treat osteoporosis safely and effectively.

Sclerostin, mainly secreted by osteocytes, has become an attractive therapeutic target for osteoporosis treatment [10,11]. Anti-sclerostin monoclonal antibodies show some effectiveness in reducing sclerostin and reactivating osteoblasts, increasing bone mass and strength [12,13]. However, antibodies have potential immunogenicity, high production cost, and poor reproducibility. The recently developed DNA aptamers, which are short single-stranded DNAs (ssDNAs) with excellent binding ability to target molecules and can avoid the inherent flaws of antibodies, bring a new opportunity for bone-targeted osteoporosis therapy. Here, we report on a novel, and simply synthesized bone-targeting nanomedicine (DNA-

* Correspondence to: No. 22, Zhongguancun South Avenue, Haidian District, Beijing 100081, PR China.

E-mail addresses: yuting.niu@bjmu.edu.cn (Y. Niu), orthoyan@bjmu.edu.cn (Y. Liu), liuyunsong@hsc.pku.edu.cn (Y. Liu), kqzhouysh@hsc.pku.edu.cn (Y. Zhou).

¹ Yuting Niu and Yang Yang contributed equally to this work.

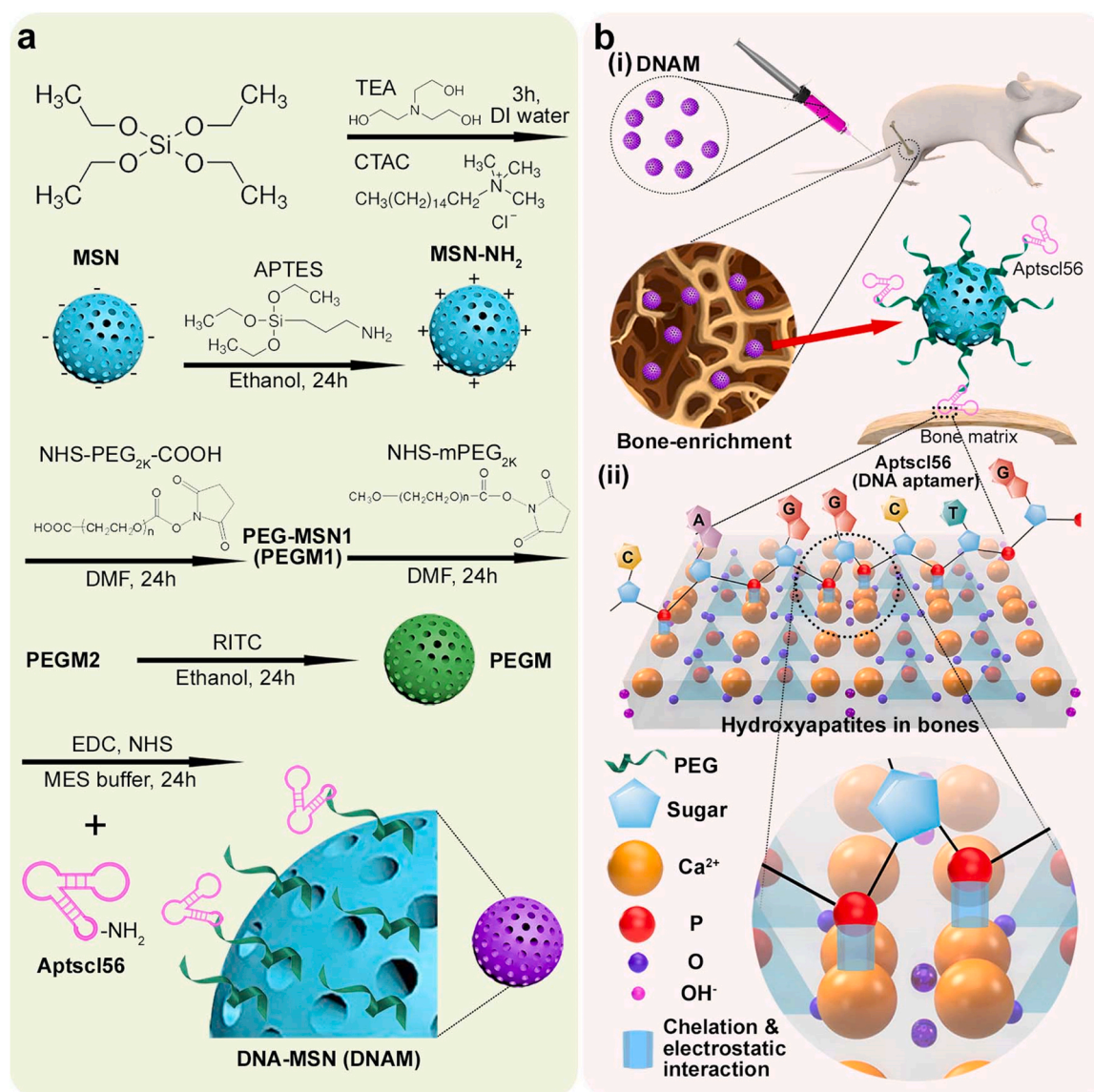


Fig. 1. Synthesis of DNAM and application of DNA aptamers as bone-targeting ligands. a) Schematic showing MSN fabrication and synthesis steps of DNAM by surface-modified dendritic MSN with anti-sclerostin DNA aptamers (Aptsc156) following amination (MSN-NH₂) and PEGylation (PEGM). DI water: deionized water; MES: 2-(N-morpholino) ethanesulfonic acid; EDC: N-Ethyl-N'-(3-dimethylaminopropyl) carbodiimide hydrochloride; NHS: N-hydroxysuccinimide; RITC: rhodamine B isothiocyanate; DMF: Dimethylformamide. b) Illustration of (i) the concept of bone-targeted nanomedicines (DNAM) for therapeutic actions. Schematic illustrating (ii) the mechanism of the bone-targeting ability of nucleic acids (*i.e.*, DNA aptamers), where phosphate groups bind with bone calcium in hydroxyapatites by chelation and electrostatic interactions.

MSN, DNAM) containing an FDA-approved anti-sclerostin DNA aptamer layer, Aptsc156 [14], and a PEGylated dendritic mesoporous silica nanoparticle (MSN) core (Fig. 1a). We show DNAM effectively reverses osteoporotic bone loss of ovariectomized (OVX) mice to a normal level, superior to the "gold standard" drug ALN. Mechanistically, the bone-targeting ability is universal and attributed to the chelation reaction and electrostatic interaction between phosphate groups in the attached Aptsc156 and bone calcium in hydroxyapatites (HA, Fig. 1b). The DNAM-immobilized Aptsc156 also enables a dual function to effectively *in situ* capture sclerostin with picomolar affinities. In addition, the nanoparticle core protects the attached Aptsc156 from rapid nuclease degradation and renal filtration, prolonging *in vivo* half-lives. Therefore, DNAM sustainably achieves bone enrichment and reduction of sclerostin, improving bone histomorphology parameters and mechanical properties in the femur, and recovering serum levels of bone turnover markers. Notably, the effective dose of DNAM-immobilized Aptsc156 is only 25% of free Aptsc156.

Results

DNAM synthesis and characterization

The innovatively developed DNAM contained a PEGylated MSN core and an Aptsc156 layer (Fig. 1a). MSNs have excellent biocompatibility [15,16], nano-scaled sizes, mesoporous structures (2–50 nm), and the ease of functionalization, and they were applied as a nanoplatform to immobilize Aptsc156 in this study. The MSN core was fabricated using a modified approach of the one-pot bi-phase stratification [17]. Scanning electron microscopy (SEM) images (Fig. S1) showed that the MSN samples after 3-, 12- and 24-hour reactions possessed uniform sizes of around 65, 90 and 150 nm, respectively. In order to enable nanomedicine extravasation from the pores (80–100 nm) in fenestrated capillaries in bone tissues [18], the 3-hour MSN sample was selected for the following experiments. Transmission electron microscopy (TEM) (Fig. S2) demonstrated that the MSN had a homogeneous morphology and a dendritic structure

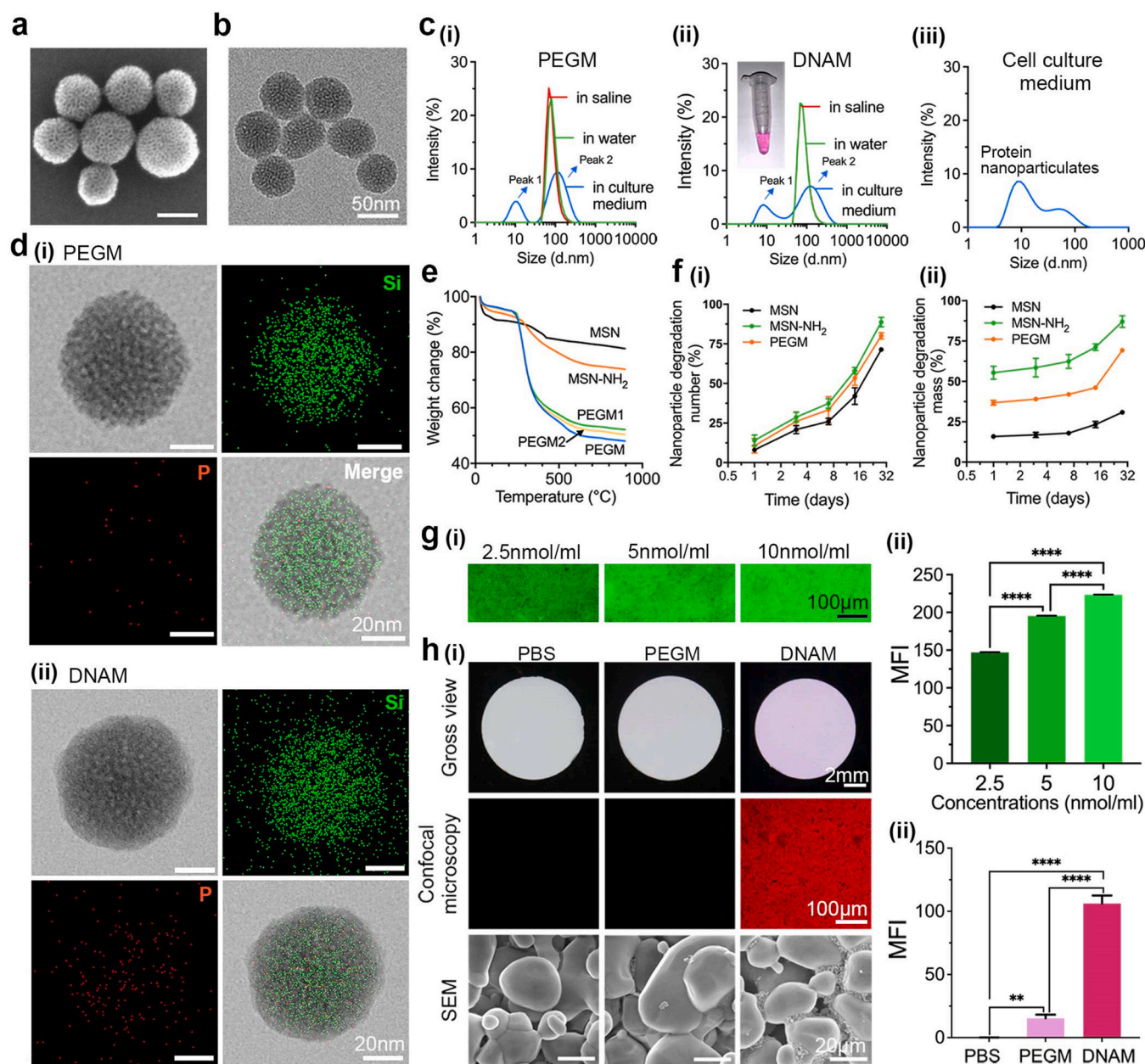
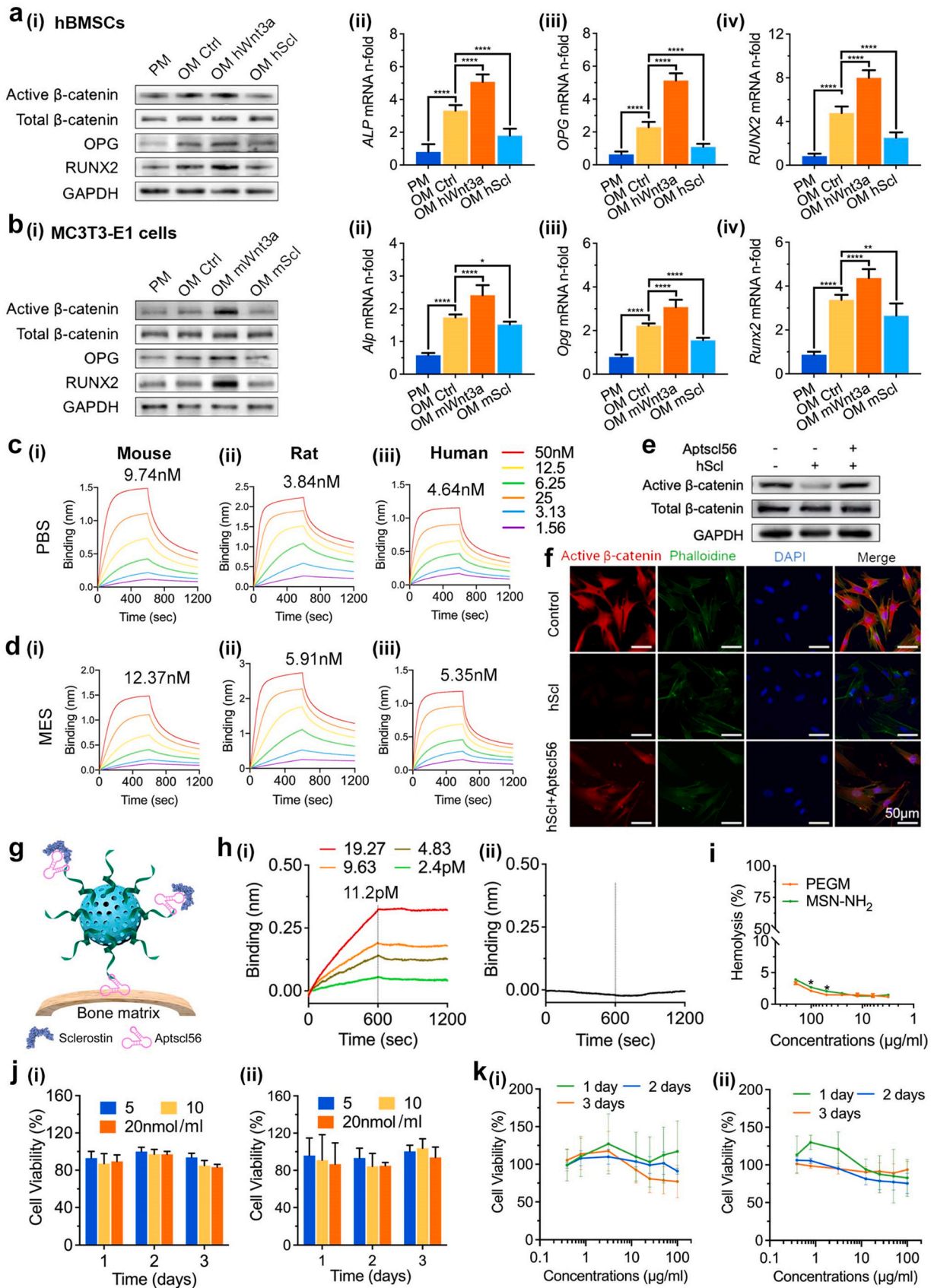


Fig. 2. Physicochemical properties of DNAM. a, b) SEM (a) and TEM (b) images showing the nanomorphology of DNAM. c) Size distribution curves of (i) PEGM and (ii) DNAM in DI water, saline and cell culture medium, respectively, and that of (iii) protein nanoparticulates in cell culture medium. Inset: DNAM is well-dispersed in saline. d) Elemental mapping of (i) PEGM and (ii) DNAM using a bright-field TEM-based energy-dispersive X-ray spectroscopy (EDX), indicating Silicon (Si) and Phosphorous (P) distributions. e) TGA curves demonstrating the quantitative analysis of nanoparticles. f) Quantitative degradation curves of nanoparticles in PBS at different incubation intervals by (i) number of nanospheres and (ii) silica mass. g) The attachment of FAM-Aptsc156 on HA tablets tested by (i) confocal microscopy and (ii) their quantification. MFI: mean fluorescence intensity. h) DNAM attachment on HA tablets tested by (i) digital imaging, confocal microscopy and SEM, and (ii) the quantification of fluorescence, compared with PEGM. Statistical significance was assessed by one-way ANOVA, $n = 3$ independent experiments in all panels. Data are represented as the mean \pm SD. * $P < 0.05$, ** $P < 0.01$, *** $P < 0.001$, and **** $P < 0.0001$.

with a mean size of 65 ± 2.35 nm (Table S1). DNAM synthesis was simple and straightforward. Due to the silanol groups on the surface, the MSN (ζ -potential: -35 mV) can be easily aminated (MSN-NH₂, ζ -potential: 29 mV, Fig. S2) for covalent conjugation with poly (ethylene glycol) (PEG)-derivatives. Nitrogen sorption (Fig. S2) confirmed a slight shrink of the mesopores in MSN-NH₂ (~ 2.5 nm) after the amine-silica coating on the MSN (~ 3.5 nm). Since both sclerostin

proteins (~ 22 kD) and the Aptscl56 (12896.4 g/mol) have dimensions of several nanometers, the mesopores were not large enough and not designed to conjugate Aptscl56 and contain captured sclerostin proteins in this study. PEG-derivatives as passivating and functional macromolecules were grafted onto MSN-NH₂ to fabricate the nanovector of PEG-MSN (PEGM, ζ -potential: 14 mV), followed by the incorporation of rhodamine B isothiocyanate for tracking and



(caption on next page)

Fig. 3. The potential of DNAM-immobilized Aptscl56 in promoting osteogenesis. a, b) Effects of (a) human and (b) mouse Wnt3a and sclerostin proteins, respectively, on osteogenesis-related (i) protein expression by Western blotting and (ii-iv) mRNA expression by RT-PCR. Ctrl: control; Scl: sclerostin; PM: proliferation medium; OM: osteogenic medium. c, d) BLI evaluating the binding kinetics of sclerostin proteins in three different species with free Aptscl56, which was treated in (c) PBS or (d) MES buffers. e, f) Intracellular accumulation of β -catenin in the cytoplasm of hBMSCs tested by (e) Western blotting and (f) confocal microscopy. g) Schematic illustrating the dual functions of DNAM to target bones and capture sclerostin. h) BLI evaluating the binding kinetics of hScl with (i) DNAM and (ii) PEGM, respectively. i) Hemolysis of nanoparticles on erythrocytes in ICR mice. j, k) Cytotoxicity of (j) free Aptscl56 and (k) DNAM to (i) hBMSCs and (ii) MC3T3-E1 cells, respectively. Statistical significance was assessed by one-way ANOVA, $n = 3$ independent experiments in all panels. Data are represented as the mean \pm SD. * $P < 0.05$, ** $P < 0.01$, *** $P < 0.001$, and **** $P < 0.0001$.

imaging. Finally, DNAM (ζ -potential: -21 mV) was acquired by covalently immobilizing Aptscl56 (ζ -potential: -34 mV) onto PEGM [19].

DNAM was characterized by various techniques. SEM (Fig. 2) and TEM (Fig. 2b) images showed that DNAM maintained the homogeneous morphology and the dendritic structure without a significant size change (~ 65 nm). Dynamic light scattering (DLS) results demonstrated DNAM and all other nanoparticles had excellent mono-dispersibility (Fig. 2c, Fig. S3, Table S1) in deionized (DI) water and saline (inset). However, because of the colloidal stabilizing ability of PEGylated surfaces, only PEGM and DNAM were well-dispersed in cell culture medium, where peak-1 represented protein nanoparticulates in fetal bovine serum (FBS), and peak-2 demonstrated narrow size distributions of PEGM or DNAM. TEM mapping (Fig. 2d) qualitatively confirmed the existence of phosphorus (P) signals derived from the phosphate backbone of Aptscl56. PEGM showed only background signals, while DNAM indicated highly concentrated P signals. Sequential quantifications, for example, ninhydrin assay, thermogravimetric analysis (TGA, Fig. 2e) and malachite green phosphate assay were conducted to trace DNAM synthesis. Importantly, every 50 nmol of Aptscl56 was immobilized to 1 mg of PEGM, equivalent to ~ 3 Aptscl56 molecules on each DNAM nanosphere. (See details in Supporting Information).

Appropriate biodegradability is important for DNAM to prolong treatment and reduce systemic toxicity, beneficial for *in vivo* studies and clinical application in the future [20]. Due to the silica nature, conventional MSNs and solid silica nanoparticles lack biodegradability. Dendritic MSNs have shown excellent biodegradability because of thin pore walls and amorphous structures [17,21]. The degradation performance of PEGM (Fig. 2f), acting as the nanovector of Aptscl56, in phosphate buffer saline (PBS) was monitored for 28 days, compared with MSN and MSN-NH₂. TEM images (Fig. S4) showed all nanospheres degraded in a trend from outside to inside. The number of nanospheres with a tendency to degrade was recorded, and the mass of degraded silica in PBS was also quantified. The PEGylated surface alleviated the disintegration rate of PEGM, reaching $\sim 80\%$ degradation by number and $\sim 69\%$ by mass, compared to the relatively slow degradation of MSN ($\sim 71\%$ & $\sim 31\%$) and the fast collapse of MSN-NH₂ ($\sim 89\%$ & $\sim 87\%$).

Effective bone-targeted delivery of Aptscl56 is one of the pivots in this study. An alendronic acid molecule has been widely used as an *in vivo* bone-targeting ligand, because diphosphonate groups can chelate with bone calcium in HA [22,23]. In addition, nucleic acids with phosphate backbones, such as DNA aptamers, have been reported to absorb on HA surfaces due to electrostatic forces [24]. Therefore, we assumed the application of DNA aptamer Aptscl56 as a safe and universal bone-targeting ligand, which has not been reported (Fig. 1b). Since each Aptscl56 molecule possesses multiple phosphate groups, the bone-binding ability is expected to be strong. To confirm this *in vitro*, we incubated FAM (a fluorescent dye)-labeled free Aptscl56 (FAM-Aptscl56) of different concentrations (2.5, 5 and 10 nmol/ml) with HA tablets, and the attachment of FAM-Aptscl56 to the HA surface increased by up to 50% in a dose-dependent manner (Fig. 2g). Moreover, we immersed HA tablets in the suspension of DNAM to verify bone-targeting performance. SEM showed evident DNAM accumulation, and fluorescence on HA tablets derived from DNAM was about seven times as much as PEGM,

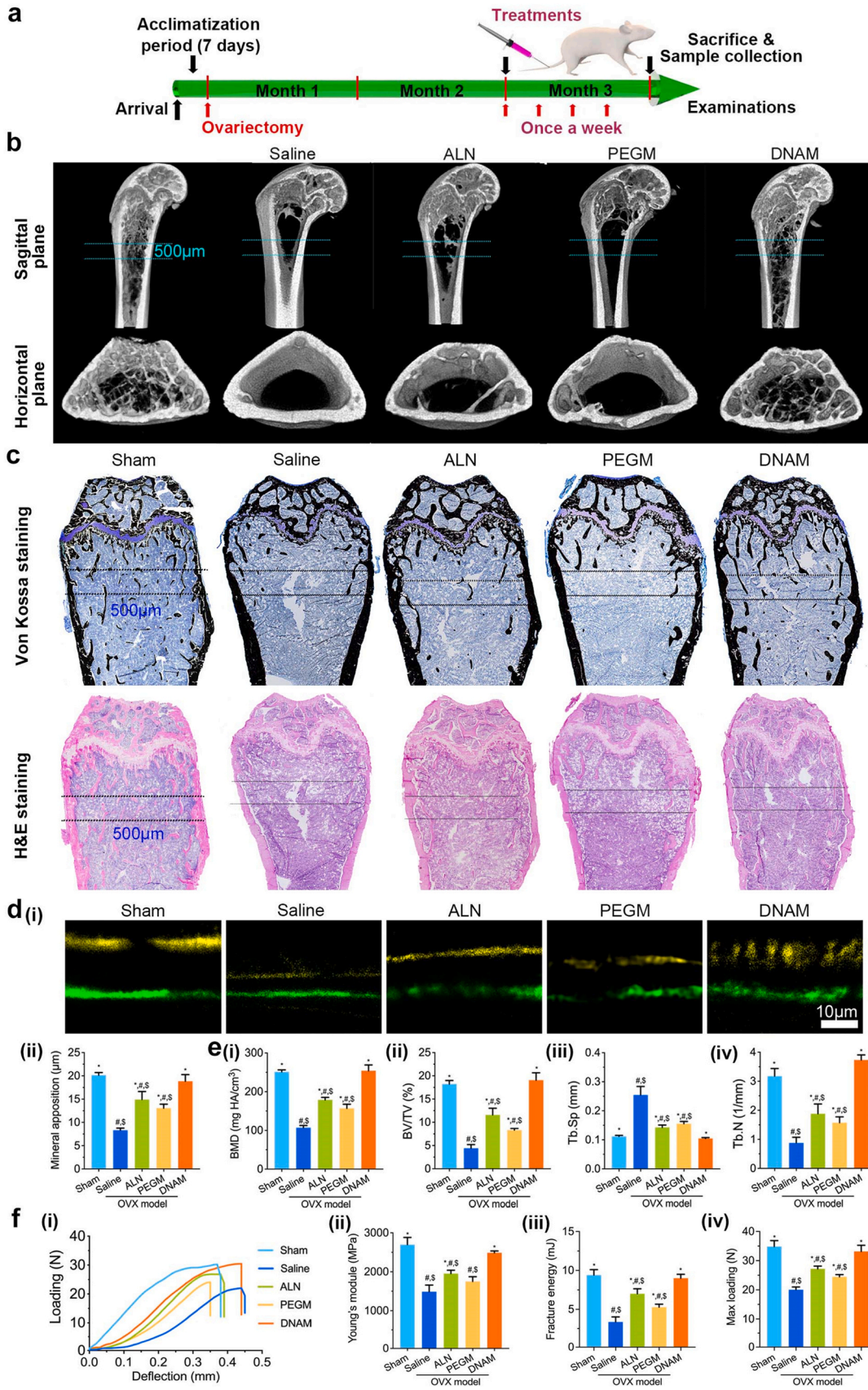
indicating DNAM-immobilized Aptscl56 was an excellent bone-targeting ligand (Fig. 2h).

The potential of DNAM-immobilized Aptscl56 in promoting osteogenesis

Sclerostin can antagonize the Wnt signaling in osteoblasts and inhibit bone formation [25], while the reduction of sclerostin can reactivate the Wnt signaling in osteoblasts and promote osteogenesis [26,27]. We first confirmed sclerostin proteins could antagonize the Wnt signaling (Fig. 3a,b) in both mouse pre-osteoblasts (MC3T3-E1 cells) and human bone marrow mesenchymal stem cells (hBMSCs), whose osteogenicity was demonstrated by Alizarin Red S staining (Fig. S5). They inhibited osteogenesis by phosphorylating a key downstream effector of β -catenin, which would be subsequently degraded [11]. In addition, protein expression of runt-related transcription factor 2 (RUNX2), a key osteogenic transcription factor, and osteoprotegerin (OPG), a cytokine inhibiting bone resorption, were also decreased. In contrast, Wnt ligands, such as mouse/human Wnt3a (mWnt3a/hWnt3a), upregulated non-phospho (active) β -catenin and enhanced protein expression of RUNX2 and OPG. Osteogenesis-related gene expression (Fig. 3a,b) in mouse and human cells exhibited consistent trends with proteins, including mouse/human alkaline phosphatase (*Alp/ALP*), a key enzyme for skeletal mineralization, *Runx2/RUNX2* and *Opg/OPG*, respectively.

To verify the capture ability of free Aptscl56 and DNAM to sclerostin, bio-layer interferometry (BLI) assays were conducted. Biotin-labeled free Aptscl56 (Biotin-Aptscl56) was treated in either PBS (pH 7.4) to simulate a physiological environment (Fig. 3c) or in MES buffer (pH 6) to reproduce the Aptscl56-grafting condition (Fig. 3d). Mouse (mScl), human (hScl) and rat sclerostin protein (rScl), respectively, bound to Biotin-Aptscl56 in PBS with nanomolar affinities ($K_{D-mScl} = 9.74$ nM, $K_{D-rScl} = 3.84$ nM and $K_{D-hScl} = 4.64$ nM). Binding kinetics was not apparently influenced after incubating in MES buffer ($K_{D-mScl} = 12.37$ nM, $K_{D-rScl} = 5.91$ nM and $K_{D-hScl} = 5.35$ nM). However, affinities were significantly weakened ($K_{D-mScl} = 14.96$ nM, $K_{D-rScl} = 8.98$ nM and $K_{D-hScl} = 9.12$ nM) in pH 2 hydrochloric acid (Fig. S6), suggesting the need for better protection of oral formulations in future research. Moreover, the presence of free Aptscl56 effectively recovered active β -catenin in the cytoplasm of hBMSCs (Fig. 3e,f). DNAM-immobilized Aptscl56 not only enabled bone-targeting, but it also exhibited a dual function to capture sclerostin (Fig. 3g). BLI results (Fig. 3h, Fig. S7) showed the affinity of DNAM to hScl was as high as 11.2 pM, independent of PEGM. Importantly, we quantified every 100 μ g of DNAM captured 2.18 ± 0.09 μ g of hScl.

Cytotoxicity of DNAM, as well as control therapeutics, was then evaluated. When DNAM is intravenously injected, it will first interact with erythrocytes. We incubated ICR mice erythrocytes with the nanovector, PEGM, compared with MSN-NH₂. Both nanoparticles (Fig. 3i) induced low hemolysis ($< 4\%$), and PEGM showed a further reduction ($< 3\%$) at high concentrations, because PEGylated surfaces can enhance hydrophilicity and reduce damages to erythrocytes [28]. We then co-cultured nanoparticles (*i.e.*, MSN-NH₂, PEGM and DNAM), therapeutic agents (*i.e.*, Aptscl56 and ALN), and dissociated silicate with MC3T3-E1 cells or hBMSCs for three days. On the whole, cell viability showed a decreasing trend with increasing doses and time. Free Aptscl56 (Fig. 3j, $> 85\%$), DNAM (Fig. 3k, $> 75\%$), as well as



(caption on next page)

Fig. 4. DNAM reverses bone loss of osteoporotic mice. a) Schematic showing the design of animal studies. b, c) Representative (b) μ CT-reconstructed 3D images and (c) histological investigations of undecalcified bone tissue sections from distal femoral metaphyseal after 4-week treatment. The space with 500 μ m of thickness between the two dash lines indicates the bone tissues in the 3D images of the horizontal plane, which was 500 μ m below the growth plate. d) Sequential fluorescent labeling showing mineral apposition by (i) confocal microscopy and (ii) quantification. Green: calcein; yellow: tetracycline. e) Parameters of trabecular bone morphology of distal femoral metaphyseal, measured by μ CT after 4-week treatments. f) Mechanical investigation of the femur by three-point bending tests showing (i) the load-deflection curves, and (ii-iv) the mechanical parameters including Young's modulus, fracture energy and max loading. Statistical significance was assessed by one-way ANOVA. n = 3 mice per group in all panels. Data are represented as the mean \pm SD. $P < 0.05$, *versus Saline, #versus Sham, and $^{\$}$ versus DNAM.

silicate (Fig. S8, > 75%) showed very good safety at all concentrations in both cells. In contrast, survival rate of MC3T3-E1 cells with MSN-NH₂ and PEGM (Fig. S9) was reduced to less than 60%. Although low concentration ALN was mild (80–90%) to both cells, the viability of MC3T3-E1 cells and hBMSCs was significantly reduced to 50% and 5% at high concentrations, respectively (Fig. S8).

Collectively, DNAM possessed a well-identified mesoporous structure, mono-dispersibility, proper biodegradability and excellent biocompatibility. Importantly, DNAM-immobilized Aptscl56 had dual functions for bone-targeted penetration and the capture of sclerostin of multiple animal species with superior affinities, implying the potential to efficiently reduce sclerostin *in vivo* and treat osteoporosis with no obvious side effects.

Osteoporosis treatment by DNAM in OVX mice

The therapeutic effects of DNAM in reversing the ovariectomy-induced bone loss of ICR mice were studied. Serological results (Table S4) suggested less than 1 mg mouse⁻¹ (< 33 mg/kg) of the nanovector (PEGM) was a safe and accessible dose without weight loss (Fig. S10). For animal studies, DNAM containing 5 nmol of Aptscl56 in saline was intravenously injected into OVX mice once a week for 4 weeks (Fig. 4a). The OVX mice injected with saline (Saline) and PEGM were set as negative control groups. The "gold standard" of commercial drug ALN with a safe dose (1 μ g) and the injection of saline after sham operation (Sham) were used as positive controls. Hematoxylin and eosin (H&E) staining showed no obvious pathological changes in organs after 4-week treatments (Fig. S11).

Bone histomorphology of femurs was evaluated by micro-computerized tomography (μ CT, Fig. 4b), Von Kossa and H&E histological staining (Fig. 4c), and sequential fluorescent labeling (Fig. 4d). Reconstructed 3D and histological images of the Saline group showed a cavity in the distal femoral metaphyseal, with 108 mg HA/cm³ of trabecular bone mineral density (Tb.BMD), 4% of trabecular bone volume (BV)/total volume (TV), 0.27 mm of trabecular separation (Tb.Sp), 0.88 mm⁻¹ of trabecular number (Tb.N), and 8.33 μ m of mineral apposition (MA), indicating the success of osteoporotic mice model and dramatic bone loss (Fig. 4e, Table S5). As expected, DNAM rescued osteoporotic bone loss, significantly improving the data of Tb.BMD (254 mg HA/cm³), BV/TV (19%), Tb.Sp (0.11 mm), Tb.N (3.73 mm⁻¹) and MA (18.85 μ m), superior to PEGM and ALN (Tb.BMD: 179 mg HA/cm³, BV/TV: 12%, Tb.Sp: 0.14 mm, Tb.N: 1.88 mm⁻¹ and MA: 14.93 μ m). Importantly, the DNAM group exhibited no statistical differences in all parameters with the Sham group (Tb.BMD: 251 mg HA/cm³, BV/TV: 18%, Tb.Sp: 0.11 mm, Tb.N: 3.17 mm⁻¹ and MA: 20.16 μ m). In addition, in the bone resorption surface, Tartrate Resistant Acid Phosphatase (TRAP) staining (Fig. S12) showed a significantly increased number of multinucleated TRAP⁺ osteoclast-like cells in the Saline group (~ 285 per mm²), compared to the Sham group (~ 53 per mm²) and the DNAM group (~ 44 per mm²).

Next, bone strength recovery was evaluated. The mechanical properties of the femurs (Fig. 4f, Table S5) in the Saline group were dramatically reduced, including Young's modulus of 1490 MPa, max

loading of 20 N and fracture energy of 3.39 mJ, compared with the Sham group (Young's modulus: 2699 MPa, max loading: 35 N and fracture energy: 9.41 mJ). After DNAM treatment, these parameters were effectively restored (Young's modulus: 2489 MPa; max loading: 33 N and fracture energy: 9.01 mJ), superior to PEGM treatment and ALN treatment (Young's modulus: 1955 MPa, max loading: 27 N and fracture energy: 7.01 mJ).

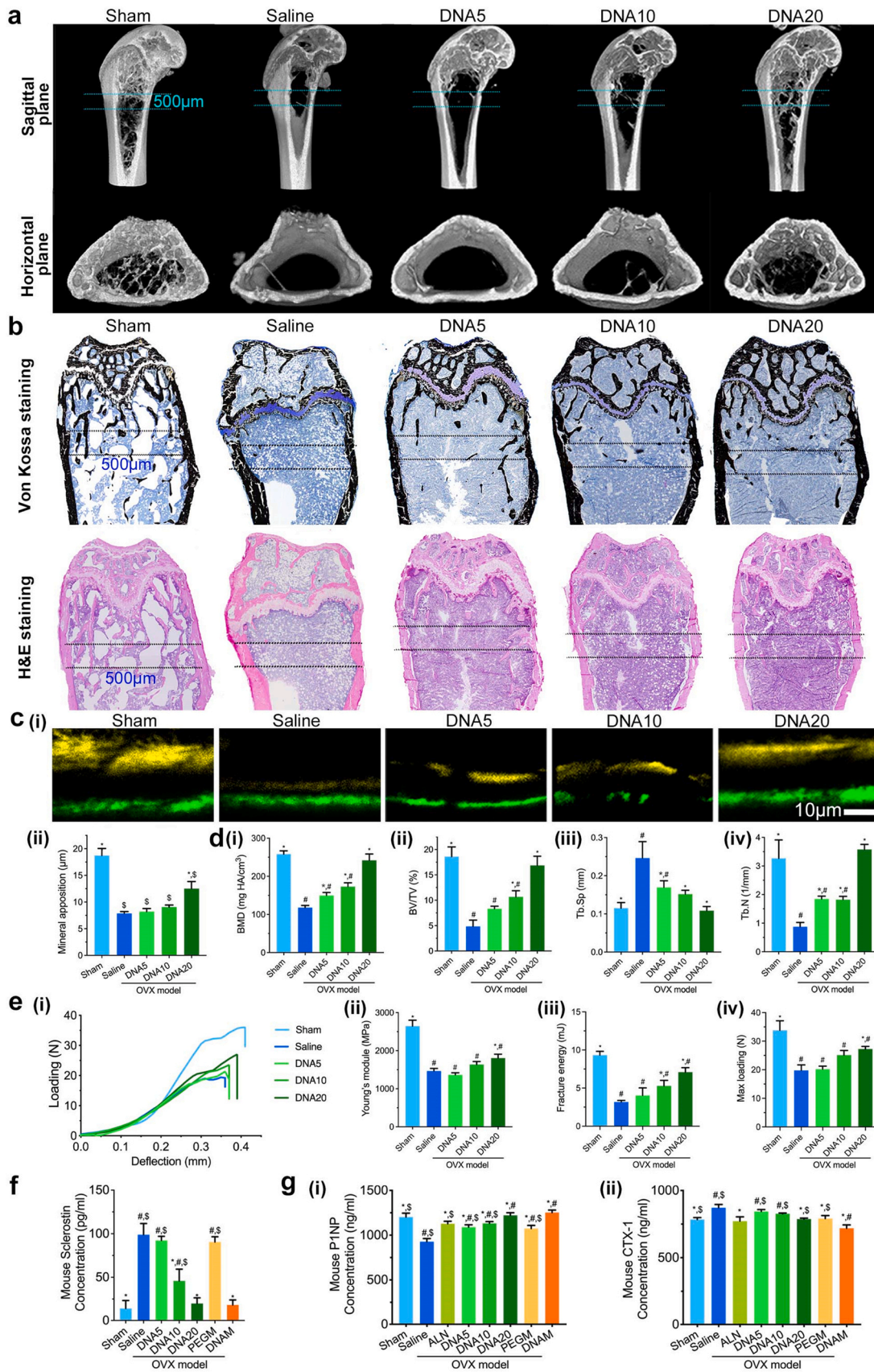
Comparing the therapeutic role of free Aptscl56 with DNAM in osteoporosis treatment

To understand why DNAM can efficiently rescue osteoporotic bone loss, we verified the therapeutic effect of free Aptscl56 of different doses, including 5 (DNA5), 10 (DNA10) and 20 nmol (DNA20). Although Aptscl56 has been used to bind sclerostin and improve the phenotype of osteogenesis imperfecta without obvious side effects, approved as the Orphan Medicinal Products by the FDA [14], it has not been applied for osteoporosis treatment. Free Aptscl56 promoted trabecular bone formation in a dose-dependent manner (Fig. 5a,b, Table S6). Although the DNAM group (Fig. 4) contained only 5 nmol of Aptscl56, it was superior to DNA5 (Tb.BMD: 150 mg HA/cm³, BV/TV: 8%, Tb.Sp: 0.17 mm, Tb.N: 1.85 mm⁻¹ and MA: 8.22 μ m; Young's modulus: 1364 MPa, max loading: 20 N and fracture energy: 4.03 mJ), and even better than DNA20 (Tb.BMD: 242 mg HA/cm³, BV/TV: 17%, Tb.Sp: 0.11 mm and Tb.N: 3.58 mm⁻¹ and MA: 12.53 μ m; Young's modulus: 1806 MPa, max loading: 27 N and fracture energy: 7.09 mJ) in bone histomorphology and mechanical properties (Fig. 5c-e). These results indicated the therapeutic role of Aptscl56 in treating osteoporosis, however, the effective dose of DNAM-immobilized Aptscl56 was only 25% of free Aptscl56.

Effective reduction of sclerostin is an important aim in this study. We investigated the changes of serum sclerostin of osteoporotic mice in response to 4-week treatments (Fig. 5f). The serum level of sclerostin in the Sham group was 14 pg/ml, and it dramatically increased to 99 pg/ml in the Saline group, implying intensive inhibition of the Wnt signaling. Inoculability quantity of free Aptscl56 dominated therapeutic effects. The DNA5 group exhibited a limited reduction of sclerostin (92 pg/ml), while the level of sclerostin was markedly reduced to 46 pg/ml in the DNA10 group and 20 pg/ml in the DNA20 group, respectively. As expected, DNAM effectively recovered the serum sclerostin level (18 pg/ml), independent of PEGM (91 pg/ml). In addition, compared to the Saline group, DNAM significantly improved serum levels of bone turnover markers (Fig. 5g), increasing procollagen type 1 N-terminal propeptide (P1NP) from 927 ng/ml to 1253 ng/ml (the Sham group: 1203 ng/ml) for bone formation, and suppressing C-terminal telopeptide of type I collagen (CTX-1) from 872 ng/ml to 719 ng/ml (the Sham group: 784 ng/ml) for bone resorption.

Mechanism of DNAM for enhanced osteoporosis treatment

We further investigated the mechanism of DNAM to improve osteoporosis treatment. Free aptamers have short *in vivo* half-lives since they are susceptible to nucleases (Fig. 6a), and they may



(caption on next page)

Fig. 5. Comparing the therapeutic role of free Aptscl56 with DNAM in osteoporosis treatment. a, b) Representative (a) μ CT-reconstructed 3D images and (b) histological investigations of undecalcified bone tissue sections from distal femoral metaphyseal after 4-week treatment. The space with 500 μ m of thickness between the two dash lines indicates the bone tissues in the 3D images of the horizontal plane, which was 500 μ m below the growth plate. c) Sequential fluorescent labeling showing mineral apposition by (i) confocal microscopy and (ii) quantification. Green: calcein; yellow: tetracycline. d) Parameters of trabecular bone morphology of distal femoral metaphyseal, measured by μ CT after 4-week treatments. e) Mechanical investigation of the femur by three-point bending tests showing (i) the load-deflection curves, and (ii-iv) the mechanical parameters including Young's modulus, fracture energy and max loading. f) Serum level of sclerostin in mice. g) Serum levels of bone turnover markers of (i) P1NP and (ii) CTX-1 in mice. Statistical significance was assessed by one-way ANOVA. n = 3 mice per group in all panels. Data are represented as the mean \pm SD. P < 0.05, *versus Saline, #versus Sham, and [§]versus DNAM.

encounter renal filtration due to their small molecular (6–30 kD) and physical sizes (<5 nm in diameter) [29]. We first evaluated the resistance of free Aptscl56 and DNAM to DNase I, respectively. Results from the agarose gel electrophoresis (Fig. 6b) exhibited that ~72% of free Aptscl56 was degraded at 15 min, and the degradation rate continuously increased to ~76% at 30 min, ~81% at 1 h, ~83% at 2 h, and finally ~92% at 24 h. In contrast, only a small portion (<47%) of DNAM-immobilized Aptscl56 was degraded with no statistical differences among all time points. The protectivity of DNAM results from its negative ζ -potential (Fig. 6a, Table S1), which shields the proximity of DNase I (isoelectric point of 5.0) having negative charges. Although free Aptscl56 also have negative charges, derived from the phosphate backbone, its electric potential is not strong enough to resist DNase I. (See details in Supporting Information).

We then investigated the biodistribution of free Aptscl56, PEGM and DNAM by *ex vivo* imaging (Fig. 6c), respectively. Their accumulation in organs (Fig. S13), such as livers and spleens, the primary organs of reticuloendothelial systems (RES) [30], and blood retention of nanoparticles (Fig. S14) were discussed in Supporting text in Supporting Information. Notably, the strongest fluorescence of Cy3 (a fluorescent dye)-labeled free Aptscl56 (Cy3-Aptscl56) was observed in the kidney at 1 h (Fig. 6c). This demonstrated rapid renal filtration of Cy3-Aptscl56, which was also monitored by the change in urine color (Fig. S15) from turbid orange at 1 h to clear yellow at 7 d. Cy3-Aptscl56 was intensively enriched in bones at 1 h (Fig. 6c), confirming our hypothesis of bone-targeted attachment. However, the fluorescence quickly reduced to 17% at 12 h and 11% at 7 d, due to nuclease degradation (Fig. 6d). These results explained the limited effects of free Aptscl56 to reduce sclerostin either in the circulation or inside bones in this study.

Nanoparticles revealed complex patterns of bone enrichment (Fig. 6c). PEGM was enriched in bones at 1 h and it was quickly excreted to 44% at 12 h and 19% at 7 d. Surprisingly, DNAM enhanced and prolonged bone enrichment (64% at 12 h and 39% at 7 d), because of the anchoring ability of DNAM-immobilized Aptscl56 to bones. The nanoparticle core not only prevented the attached Aptscl56 from nuclease degradation in bones (Fig. 6d), prolonging drug action, but also formulated as a bulky moiety to increase the mass above the cut-off threshold for renal glomerulus, avoiding renal filtration. The bone-penetrated DNAM was clearly observed in the distal femoral metaphyseal of OVX mice after 4-week treatment, *in situ* promoting bone formation (Fig. 6e). Released silicate from DNAM was also beneficial for osteogenesis by increasing protein expression of OPG and RUNX2 (Fig. S16).

In brief, DNAM orchestrated different effects, including the prevention of immobilized Aptscl56 from nuclease degradation and renal filtration, the bone-targeted penetration for *in situ* capture/reduction of sclerostin with picomolar affinities, promoting bone formation sustainably. Although a portion of DNAM was confined in the liver and spleen, the MSN core was expected to protect the attached Aptscl56 from quick degradation. In that case, the DNAM in the liver and spleen can still capture sclerostin in the blood circulation. The decreased DNAM fluorescence in the liver and spleen demonstrated that DNAM-sclerostin complexes were gradually

excreted through the intestines and feces [31], decreasing the dose-dependent systemic toxicity. DNAM has performed as a multifunctional nanosystem to effectively and safely improve osteoporosis treatment.

Discussion

Bone-targeted treatments of osteoporosis remain a major challenge. Existing nanomedicine [32] strategies to treat osteoporosis encounter various obstacles. Using viral [33] or non-viral nanocarriers [34,35], conventional drugs are delivered into either osteoblasts or osteoclasts, which can cause unpredictable side effects due to the inability to precisely control cellular internalization of nanoparticles and drug doses. Here, the innovatively developed DNAM can avoid these drawbacks by regulating unwanted circulating biohazards of sclerostin *via* nanotechnology. Recent studies have used alendronic acid molecules [23], tetracyclines [36] or oligopeptides (*i.e.*, Asp₁₄ [33]) as bone-targeting ligands. However, ALN can induce hypocalcemia, nephrotoxicity and osteonecrosis of the jaw [37], and tetracycline can incorporate into and stain active mineralization sites, such as dental and bone tissues [38]. Although oligopeptides of multi-aspartic acids are relatively safe, their strong negative charges hinder the synthesis. Depending on the DNA nature having phosphate backbones, we applied a DNA aptamer as a novel and universal bone-targeting ligand to effectively direct bone enrichment of nanomedicines. In addition, the monodispersibility of nanoparticles in the blood is an important prerequisite for systemic administration, since protein corona on nanoparticles will induce aggregation, resulting in blockage of blood vessels or rapid excretion from the body [39]. DNAM equipped with the PEGylated surface and the Aptscl56 layer exhibited strong negative charges and hydrophilicity to propel serum proteins. Therefore, DNAM was well-dispersed in physiological environments, avoiding the sonication processes for de-agglomerating nanomaterials while destroying the attached Aptscl56 [40].

The nanoparticle core and the Aptscl56 layer in the present study demonstrate a great collaboration for enhanced osteoporosis treatment. The nanoparticle core with excellent biocompatibility and appropriate biodegradability functioned as a nanoplatform to immobilize and protect the Aptscl56. Bone-targeting drug delivery technologies minimized systemic toxicity, and at the same time, improved the pharmacokinetic profile and therapeutic efficiency of drugs [41]. The DNAM-attached Aptscl56 not only acted as a powerful bone-targeting ligand, but also exhibited a dual function to capture sclerostin, avoiding extra modification processes. The picomolar affinity of DNAM with sclerostin was attributed to multivalent immobilization of Aptscl56. In addition, the therapeutic dose of DNAM was very low without systemic toxicity concerns. Aptscl56 possesses a small molecule weight (~13 kD), and the usage is 65–258 μ g corresponding to 5–20 nmol dosing. Therefore, only 165 μ g (containing 100 μ g of PEGM) of DNAM per mouse was intravenously injected every time in this study.

Further development of the immobilized-Aptscl56 approach may maximize osteoporosis treatment efficiency. For example, the

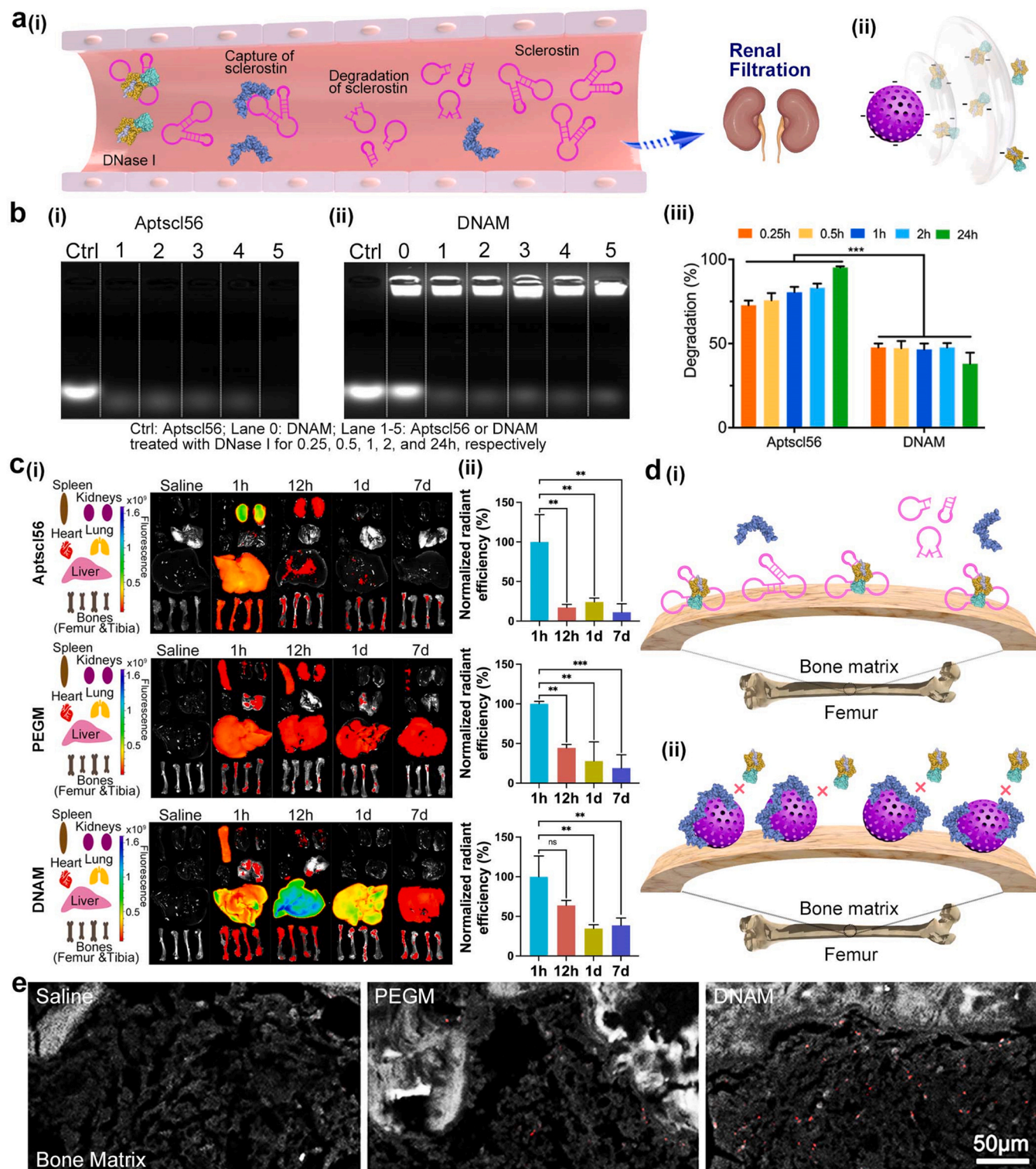


Fig. 6. DNAM rescues osteoporosis by protecting the attached Aptscl56 from nuclease degradation and rapid renal filtration. a) Schematic illustrating that (i) free Aptscl56 suffers from nuclease degradation and renal filtration and (ii) DNAM repels the proximity of DNase I. b) Representative agarose gel electrophoresis imaging of degradation processes of (i) free Aptscl56 in comparison with (ii) DNAM by DNase I and (iii) their semi-quantifications. c) After the injection of Cy3-Aptscl56, PEGM and DNAM in mice, the representative (i) *ex vivo* imaging of organs and bones and (ii) their quantified accumulation in bones at varying intervals, respectively. d) Schematic showing (i) nuclease degradation of Aptscl56 in bones and (ii) DNAM avoids being degraded in bones. e) Confocal microscopy showing intrabony distribution of PEGM and DNAM (red dots) in undecalcified bone tissue sections from distal femoral metaphyseal after 4-week treatments, respectively. White: bone matrix; red: rhodamine B on nanoparticles. Statistical significance was assessed by one-way ANOVA, $n=3$ independent experiments in all panels. Data are represented as the mean \pm SD. * $P < 0.05$, ** $P < 0.01$, *** $P < 0.001$, and **** $P < 0.0001$; ns: not significant.

optimization of Aptscl56 to nanosphere ratios may lead to an enhanced bone-targeted reduction of sclerostin. The regulation of MSN frameworks, for example, using periodic mesoporous organosilica nanoparticles (PMO) [42], can improve bio-availability and stimuli-responsive biodegradability. Moreover, oral formulations [43] can be achieved by the participation of additional components to protect Aptscl56 from damages in the digestive tract [44] and to direct intestinal uptake [45]. Aptscl56 has high specificity to sclerostin in multiple animal species, including humans, and the DNAM approach can be translated into clinical application in the future.

Conclusion

In this study, we develop a novel, and simply fabricated nanomedicine of Aptscl56-immobilized PEGylated dendritic MSN, and present a functional bone regeneration strategy in a mouse model of postmenopausal osteoporosis by bone-targeted reduction of sclerostin. Our results emphasize complementary effects between the Aptscl56 layer and the nanoparticle core in maximizing their therapeutic functions. Our data suggest a simple and translatable therapeutic strategy that improves the therapeutic effects of Aptscl56, reactivates the regenerative potential and avoids the complexity of the delivery system.

Methods

Nanomedicine synthesis and characterizations

Synthesis of MSN

The dendritic MSN were formed using one-pot biphasic stratification approach with modification, using tetraethyl orthosilicate (TEOS, Macklin) as a silica source, cetyltrimethylammonium chloride (CTAC, Aladdin) as a template, cyclohexane (Macklin) as an emulsion agent and triethanolamine (TEA, Aladdin) as a catalyst. Typically, 48 ml of (25 wt%) CTAC solution, 0.36 g of TEA, and 72 ml of DI water were mixed in a 500 ml round bottom flask and stirred at ~ 150 rpm with a 2-cm Teflon-coated stirring bar at 60 °C for at least 1 h to form micelles. Then, the oil phase of 20 ml of (20 v/v%) TEOS solution in cyclohexane was added gently to the surface of the aqueous phase with constant stirring at 60 °C for 3 h to form the MSN. After the reaction, the milky solution in the aqueous phase was separated using a pear-shaped separating funnel, and the MSN was collected by centrifugation at 36,000 g for 90 min. The collected MSN was extracted with acid methanol (37% HCl: methanol = 1: 10) at 60 °C for 6 h three times to remove the remaining template. Finally, the MSN products were stabilized in ethanol at room temperature.

Synthesis of MSN-NH₂

Amine silane was grafted onto the MSN to provide a reactive surface for covalent conjugation with PEG-derivatives. Typically, 250 mg of the MSN was dispersed in 50 ml of ethanol with 1 ml of ammonium hydroxide (28–30%, Sigma) as a catalyst. Then, 4 ml of 3-aminopropyl triethoxysilane (APTES, Sigma) was dropwise added, stirring at 25 °C for 24 h. After the reaction, MSN-NH₂ was obtained by centrifugation, washing with ethanol to remove residual APTES and catalyst. The product was kept in ethanol for further experiment.

Synthesis of PEGM

In order to prolong the circulation time and minimize the toxicity, two PEG-derivatives with molecular weights around 2000 Da (Xi'an ruixi Biological Technology Co., Ltd) were attached on MSN-NH₂, consecutively. First, 100 mg of MSN-NH₂ were dispersed in 10 ml of dimethylformamide (DMF). In the meanwhile, 108 mg of N-hydroxysuccinimide-PEG_{2k}-carboxyl (NHS-PEG_{2k}-COOH) was dissolved in 15 ml of DMF. Then, the NHS-PEG_{2k}-COOH solution was dropwise added into the MSN-NH₂ dispersion, reacting at 25 °C for

24 h to enable click-crosslinking between an amino-group and an NHS-group, and the product was designated as PEGM1. After that, NHS-functionalized PEG_{2k} (NHS-mPEG_{2k}) was used to block unreacted amine groups, and 106 mg of NHS-mPEG_{2k} was reacted with the as-synthesized PEGM1 in 25 ml of fresh DMF at 25 °C for 24 h to fabricate PEGM2. In order to trace nanomedicine distribution, 2.5 mg of a fluorescent dye of Rhodamine B isothiocyanate (Macklin) was attached on remaining amine groups of the as-synthesized PEGM2 in 25 ml of ethanol at 25 °C for 24 h to form PEGM. This reaction was also dependent on the click-chemistry between an amine group and an isothiocyanate group. PEGM was washed and kept in ethanol for further experiment.

Synthesis of DNAM

Aptscl56 with an amine group terminal was conjugated onto PEGM to fabricate DNAM. Typically, 200 nmol of Aptscl56 was mixed with 10 mg of PEGM in 10 ml of 0.1 M 2-(N-morpholino) ethanesulfonic acid (MES, Sigma) buffer, pH6, with the addition of 0.959 mg of N-(3-Dimethyl aminopropyl)-N'-ethylcarbodiimide hydrochloride (EDC, Sigma) and 0.288 mg of N-Hydroxysuccinimide (NHS, Sigma), and they reacted at 37 °C for 24 h. The carboxylic group in PEGM was used to react with the amine group in Aptscl56. After washing DNAM with DI water, the excess liquid was drained and the final product of DNAM was kept in wet condition at 4 °C.

Amine group quantification

The amount of amine group represents the active sites for PEG-modification. Briefly, 100 µg of MSN, MSN-NH₂, PEGM1, PEGM2 and PEGM were first dispersed in 100 µl of DI water, respectively. Then, 100 µl of (2 w/v%) ninhydrin solution in dimethyl sulfoxide (DMSO, Aladdin) was mixed for chromogenic reaction at 90 °C for 20 min. After the mixtures were cooled down to room temperature, 800 µl of ethanol was added to stop the reaction, and the absorbance at 570 nm using a microplate reader (ELX808, BioTek) was recorded. Glycine solutions from 2.5 to 25 mM were used to draw a standard curve.

Characterization of the samples

The samples were subjected to SEM without coating. SEM images were taken using Hitachi Regulus 8230 microscope operating at 5 kV. For TEM measurements, the specimens were dispersed in ethanol and transferred to a copper grid. TEM images were taken using JEOL 1400 microscope operated at 100 kV. TEM-based EDX mapping for Si and P was also acquired. The TGA was conducted using a Q600 TGA-DSC-DTA Thermogravimetric Analyzer (Mettler-Toledo Inc) at a heating rate of 5 K/min in air. ζ-potential and DLS measurements were performed at 25 °C using a Zetasizer Pro (Malvern Instruments). For ζ-potential values, all samples were tested in DI water. For DLS tests, each sample was dispersed in DI water, saline, and Minimum Essential Medium Alpha Basic (α-MEM, Gibco) supplemented with 10 v/v% FBS, respectively, by proper ultrasonication. Nitrogen adsorption-desorption measurements were carried out at -196 °C to obtain information on the porosity using a Micromeritics ASAP® 2020 analyzer. The samples were degassed at 120 °C overnight on a vacuum line. The Brunauer-Emmett-Teller (BET) method was used to calculate specific surface area (A_{BET}). The pore size distribution curve was derived from the adsorption branch of the isotherms using the Barrett-Joyner-Halanda (BJH) method. The total pore volume was calculated from the amount adsorbed at maximum relative pressure (P/P₀) of 0.99.

Quantification of Aptscl56 attachment

Since each aptscl56 molecule possesses 40 phosphate groups in the backbone, the amount of attached Aptscl56 was quantified using a Malachite Green Phosphate Assay Kit (Sigma). Briefly, 100 µl of 1 mg/ml DNAM dispersion in DI water was first mixed with 200 µl of

5 M H₂SO₄ to digest DNA molecules at 100 °C for 5 h. Then, 700 µl of DI water was added to decompose the pyrophosphoric acid at 100 °C for 10 min, acquiring free orthophosphates. After centrifugation, the supernatant was collected and neutralized with 1 M NaOH, followed by mixing it with a working reagent for chromogenic reaction at room temperature. The concentration of free orthophosphate was determined based on the absorbance at 630 nm using a microplate reader, interpolating a standard curve.

Degradation of MSN, MSN-NH₂ and PEGM

To evaluate the degradability, the specimens of MSN, MSN-NH₂ and PEGM were dispersed in 10 ml of PBS at a concentration of 1 mg/ml, under constant stirring at 37 °C for 28 days. On day 1, 3, 7, 14 and 28, nanoparticle samples were collected for TEM observations. Moreover, 1000 µl of the specimens were picked up and centrifuged, and the supernatant was subjected to inductively coupled plasma optical emission spectrometry (ICP-OES) to determine the concentration of silica in PBS, which accumulates with the process of material degradation. The sediments were put back after redispersion in 1000 µl of fresh PBS, continuing the degradation process.

Binding specificity of Aptscl56 and DNAM to sclerostin

Bilayer Interferometry (BLI) assays to evaluate the affinity between Aptscl56 and sclerostin proteins were first carried out by an Octet RED96e instrument (FortéBio). Briefly, the Biotin-Aptscl56 were loaded on the streptavidin (SSA) biosensors (FortéBio), and biosensors were blocked by 0.1 wt% BSA with 0.02 v/v% Tween 20 in PBS. Then, the biosensors were respectively soaked in mScl (R&D Systems), rScl (SinoBiological) and hScl (AcroBiosystems) solutions with a series of concentrations from 1.5625 nM to 50 nM, and hold for 600 s. After the binding process, the biosensors were dissociated for 600 s. The binding responses were reported using the time-binding graph in real time. The association rate constant (k_{on}), dissociation rate constant (k_{dis}) and the equilibrium dissociation constant ($K_D = k_{dis}/k_{on}$) were calculated by the Octet data analysis software version 11.0.

For evaluating the binding specificity of DNAM to hScl, an AR2G biosensor was dipped in 25 µg/ml sclerostin proteins solution and was used to chemically conjugate sclerostin proteins onto its surface. After reaching the baseline, the sensors were subjected to an association buffer with 65–520 ng/L DNAM, corresponding to 2.4–19.27 pM DNAM-attached Aptscl56 for 240 s and then dissociated for 600 s. PEGM (520 ng/L) was used as a control. The equilibrium dissociation constants were calculated accordingly.

In addition, quantitative binding of DNAM with hScl was tested by enzyme-linked immune sorbent assays (ELISA). Briefly, 165 µg of DNAM were mixed with 4 µg of sclerostin proteins and incubated at 37 °C for 1 h. Then, the supernatant was centrifuged and subjected to ELISA tests (R&D Systems) to determine the remaining sclerostin proteins.

Agarose gel electrophoresis

Agarose gel electrophoresis imaging was used to evaluate the protective ability of DNAM to the attached Aptscl56 from DNase I, compared with free Aptscl56. Briefly, 500 nmol of free Aptscl56 and DNAM corresponding to 500 nmol of attached Aptscl56 were incubated in 50 µg/ml DNase I of 10 mM Tris-HCl buffer, pH 7.4, containing 10 mM CaCl₂ and 10 mM MgCl₂, and kept at 37 °C for 0.25, 0.5, 1, 2 and 24 h (lane 1–5), respectively. Free Aptscl56 (Ctrl) and/or DNAM (lane 0) without the addition of DNase I were used as control groups. Then, the samples were mixed with TBE-Urea loading buffer and heated at 70 °C for 10 min to denature DNase I and free ssDNA molecules. After that, samples were loaded into the wells of a 2 wt% agarose gel (LABLEAD BIOTECH), supplemented with 2 v/v% formaldehyde and 0.01 v/v% SYBR® Safe DNA gel Stain (Invitrogen). They were run in MOPS buffer (Sangon Biotech) at 3 V/cm for 1 h.

DNA molecule bands were visualized using a UV illuminator, and the intensity of each band was semi-quantified using the built-in software, and the degradation rate was normalized to the control groups.

Cell experiments

Western blotting

Protein expression was determined for cell culture groups supplemented with 1 µg/ml sclerostin, 100 ng/ml Wnt3a, 10 nmol/ml Aptscl56, sclerostin+Aptscl56 and 100 µg/ml silicate, respectively. The protein bands were detected with anti-total β-catenin, anti-non-phospho (active) β-catenin, anti-RUNX2, anti-ALP, anti-OPG and anti-GAPDH antibodies (Cell Signaling Technology) and imaged, respectively. Detailed information of primary and secondary antibodies was listed in Table S2, and original western blotting images were shown in Fig. S17.

Quantitative real-time reverse transcription PCR

MC3T3-E1 cells and hBMSCs were cultivated in 6-well plates using either PM or OM. Stimulants were added to different groups every other day. For the OM+Wnt3a groups, hWnt3a or mWnt3a protein (MedChemExpress) was added to OM at 100 ng/ml concentration. For the OM+Scl groups, the recombinant hScl or mScl were added at the concentration of 1 µg/ml. Using the glyceraldehyde-3-phosphate dehydrogenase (GAPDH) as a reference gene, the mRNA expression of RUNX2, OPG, and ALP was determined. Detailed information on primers was listed in Table S3.

Cell immunofluorescent staining

To visualize the accumulation of active β-catenin in cells, high-quality fluorescent images were acquired by confocal laser scanning microscopy (CLSM). After seeding 1×10^5 hBMSCs onto 12-mm glass coverslips in 24 well-plates, either 1 µg/ml hScl alone or the mixture of hScl and 100 ng/ml Aptscl56 was supplemented. In three days, the attached cells were first fixed with 4% paraformaldehyde in PBS for 30 min, blocked in PBS with 5 v/v% rabbit serum and 0.3 v/v% Triton X-100 for 1 h at room temperature, and incubated with anti-active β-catenin antibody in antibody buffer (1 wt% BSA and 0.3 v/v% Triton X-100 in PBS) overnight at 4 °C. Then, the cells were incubated with secondary anti-Rabbit IgG (H+L) F(ab')₂ Fragment (Cell Signaling Technology) in antibody buffer at room temperature for 1 h. After that, the cells were further incubated with FITC-phalloidin (Sigma Aldrich) in antibody buffer at room temperature for another 1 h. Finally, the coverslips were mounted onto glass slides by Fluoroshield™ with DAPI (Sigma). The slides were viewed using a confocal laser scanning microscope (LSM710, Zeiss).

Animal studies

Animals

The 6-to-8-week-old female ICR mice were purchased from the Charles River Company, Beijing, China. All animal experiments were performed following ARRIVE (Animal Research: Reporting of In Vivo Experiments) guidelines. The animal studies protocols were approved by the ethics committee of Peking University Health Science Center (Approval number: LA2019019). All mice were maintained under specific pathogen-free rooms with a 12-hour light/12-hour dark cycle. The animals were allowed access to free food pellets and tap water ad libitum.

Ovariectomy and sham operations

The ovariectomy or sham procedure was performed under general anesthesia using pentobarbital sodium (50 mg/kg). For the OVX group, the bilateral ovaries were removed. Sham surgery was

performed for the control group with ovaries left untouched. All mice were carefully sutured and given antibiotics and analgesics.

Treatments

The OVX mice were randomly divided into different groups, including the negative control group (Saline), positive control group (1 μg of alendronate sodium), nanovector group (100 μg of PEGM), DNA groups (5, 10 and 20 nmol of free Aptscl56, respectively), and DNAM group (165 μg of DNAM). The therapeutics were injected *via* a tail vein once a week for a total of 4 weeks. At the endpoint, all animals were euthanized. The whole blood, internal organs (heart, liver, lung, spleen, kidneys), and femora were collected.

μCT scanning and analysis

The mice femora were fixed with 70 v/v% ethanol for 48 h. Then the femora were scanned with a Skyscan 1174 micro-CT system (Bruker, Belgium) at a resolution of 5.9 μm . The acquired axial images were imported into NRecon and CTvox software for visualization and analysis. We defined the region of interest as the areas 0.5 distal to the proximal epiphysis, including the secondary trabecular spongiosa. Tb.BMD, BV/TV, Tb.Sp and Tb.N of the "region of interest" (ROI) for each specimen were calculated using CTAn software.

Bone histology and dynamic histomorphology

After finishing μCT analysis, hard tissue sections were acquired through the processes of dehydration, embedding in resin, and sectioning into 5–8 μm slices using a tungsten steel blade, followed by deplasticization. The mineralization of bone tissue was observed after Von Kossa and H&E staining. To determine bone formation rate (BFR), sequential fluorescent labeling of calcein (10 mg/kg, Macklin) and tetracycline (60 mg/kg, Aladdin), respectively, was intraperitoneally injected into all mice on weeks 3 and 4 during treatments. The spacing between the two fluorescent dyes was recorded.

For TRAP staining, the femur samples were fixed using 4% paraformaldehyde for 24 h and decalcified in a 10% ethylene diamine tetraacetic acid (EDTA) solution. After dehydration, the tissues were embedded in paraffin and then sectioned into 5 μm slices, followed by staining using commercial TRAP kits (Sigma-Aldrich).

Mechanical tests of femora

To evaluate the mechanical strength of mice femora, three-point bent tests were carried out using a universal mechanical testing machine (Zwick/Poell Z020). The femora were centered on the supporting platform at 25 mm apart, with the anterior surface facing up. The load was applied at the center of the femur at a 5 mm/min rate until bone fracture. Maximum loading, fracture loading, and Young's module were calculated using the built-in software.

Quantification of nanoparticles in excised organs

The excised organs were carefully weighed, stored in PBS, and minced using a high throughput tissue grinding machine (Qiagen) with steel beads. Further, the organs were completely disrupted by an ultrasonic processor. Then, NaOH solution was added to reach a final concentration of 1 M to fully dissolve the silica in PEGM and DNAM at room temperature for 24 h. After centrifugation, the supernatant of each sample was filtered and subjected to Inductively Coupled Plasma-Optical Emission Spectrometer (ICP-OES) tests to determine the concentration of silica.

Biodistribution study of therapeutics

To better understand the pharmacokinetics of different therapeutics, their biodistribution was monitored. Briefly, 20 nmol of Cy3-Aptscl56, 400 μg of PEGM, and 660 μg of DNAM in 200 μl saline, respectively, were injected into healthy female ICR mice through the tail vein, and 200 μl of saline was injected as a control group. At each

time point (1 h, 12 h, 1 d, 7 d after injection), three mice in each group were euthanized, and their internal organs (heart, liver, spleen, lung, and kidneys), femora, and tibiae were collected. The samples were subjected to *ex vivo* imaging and quantitative analysis by an IVIS Spectrum In Vivo Imaging System (PerkinElmer).

CRediT authorship contribution statement

Yuting Niu: Conceptualization, Methodology, Investigation, Software, Data curation, Visualization, Validation, Writing – original draft, Writing – review & editing, Funding acquisition. **Yang Yang:** Methodology, Investigation, Data curation, Visualization, Writing – original draft, Writing – review & editing. **Zhen Yang:** Investigation, Data curation. **Xu Wang:** Investigation, Data curation. **Ping Zhang:** Formal analysis, Validation. **Longwei Lv:** Formal analysis, Validation. **Yan Liu:** Conceptualization, Supervision, Writing – review & editing, Funding acquisition. **Yunsong Liu:** Conceptualization, Writing – review & editing, Validation. **Yongsheng Zhou:** Conceptualization, Supervision, Writing – review & editing, Funding acquisition.

Declaration of Competing Interest

The authors declare that they have no known competing financial interests or personal relationships that could have appeared to influence the work reported in this paper.

Acknowledgements

Yuting Niu and Yang Yang contributed equally to this study. We thank Dr. Hao Liu for the discussions about the project. We thank Dr. Yuan Zhu and Ms. Qinyuan Dong for their help in animal experiments. We thank Mr. Feilong Wang for his help in mechanical tests. We thank Dr. Jing Wang from the State Key Laboratory of Natural and Biomimetic Drugs, Peking University, for technical assistance on the BLI analysis. We acknowledge financial support from the National Natural Science Foundation of China, Nos. 81901054 (Yuting Niu), 81930026 (Yongsheng Zhou) and 81871492 (Yan Liu); and the China Postdoctoral Science Foundation, No. 2019M660010 (Yuting Niu).

Supporting information

Supporting methods for more details are prepared in the Supporting Information

Appendix A. Supporting information

Supplementary data associated with this article can be found in the online version at doi:10.1016/j.nantod.2022.101529.

References

- [1] I.R. Reid, A broader strategy for osteoporosis interventions, *Nat. Rev. Endocrinol.* 16 (2020) 333–339, <https://doi.org/10.1038/s41574-020-0339-7>
- [2] Q. Zeng, N. Li, Q. Wang, J. Feng, D. Sun, Q. Zhang, J. Huang, Q. Wen, R. Hu, L. Wang, Y. Ma, X. Fu, S. Dong, X. Cheng, The prevalence of osteoporosis in China, a nationwide, multicenter DXA survey, *J. Bone Miner. Res.* 34 (2019) 1789–1797, <https://doi.org/10.1002/jbmr.3757>
- [3] A. Salhotra, H.N. Shah, B. Levi, M.T. Longaker, Mechanisms of bone development and repair, *Nat. Rev. Mol. Cell Biol.* 21 (2020) 696–711, <https://doi.org/10.1038/s41580-020-00279-w>
- [4] M. Rabiei, S. Kashanian, S.S. Samavati, H. Derakhshankhah, S. Jamasb, S.J.P. McInnes, Nanotechnology application in drug delivery to osteoarthritis (OA), rheumatoid arthritis (RA), and osteoporosis (OSP), *J. Drug Deliv. Sci. Tec.* 61 (2021) 102011, <https://doi.org/10.1016/j.jddst.2020.102011>
- [5] X. Sun, J. Wei, J. Lyu, T. Bian, Z. Liu, J. Huang, F. Pi, C. Li, Z. Zhong, Bone-targeting drug delivery system of biomineral-binding liposomes loaded with icariin enhances the treatment for osteoporosis, *J. Nanobiotechnol.* 17 (2019) 10, <https://doi.org/10.1186/s12951-019-0447-5>
- [6] Y. Kim, Y. Tian, J. Yang, V. Huser, P. Jin, C.G. Lambert, H. Park, S.C. You, R.W. Park, P.R. Rijnbeek, M. Van Zandt, C. Reich, R. Vashisht, Y. Wu, J. Duke, G. Hripcsak,

- D. Madigan, N.H. Shah, P.B. Ryan, M.J. Schuemie, M.A. Suchard, Comparative safety and effectiveness of alendronate versus raloxifene in women with osteoporosis, *Sci. Rep.* 10 (2020) 11115, <https://doi.org/10.1038/s41598-020-68037-8>
- [7] N. Nuti, N. Baldini, C. D'Elia, G. Gabriele, P. Gennaro, M. Ferrari, Dental implants in osteoporotic patients taking oral bisphosphonates: a literature review, *Clin. Cases Miner. Bon* 15 (2018) 183–189, <https://doi.org/10.11138/ccmbm/2018.15.2.183>
- [8] M.A. Figueiredo, F.B. Medeiros, K.L. Ortega, Osteonecrosis of the jaw in a patient under treatment of osteoporosis with oral bisphosphonate, *Autops. Case Rep.* 11 (2020) e2020186, <https://doi.org/10.4322/acr.2020.186>
- [9] S. Minisola, C. Cipriani, G.D. Grotta, L. Colangelo, M. Occhiuto, P. Biondi, C. Sonato, E. Vigna, M. Cilli, J. Pepe, Update on the safety and efficacy of teriparatide in the treatment of osteoporosis, *Ther. Adv. Musculoskel. Dis.* 11 (2019), <https://doi.org/10.1177/1759720X19877994>
- [10] J. Kim, W. Han, T. Park, E.J. Kim, I. Bang, H.S. Lee, Y. Jeong, K. Roh, J. Kim, J.-S. Kim, C. Kang, C. Seok, J.-K. Han, H.-J. Choi, Sclerostin inhibits Wnt signaling through tandem interaction with two LRP6 ectodomains, *Nat. Commun.* 11 (2020) 5357, <https://doi.org/10.1038/s41467-020-19155-4>
- [11] J. Peng, Z. Dong, Z. Hui, W. Aifei, D. Lianfu, X. Youjia, Bone sclerostin and dickkopf-related protein-1 are positively correlated with bone mineral density, bone microarchitecture, and bone strength in postmenopausal osteoporosis, *BMC Musculoskel. Disord.* 22 (2021) 480, <https://doi.org/10.1186/s12891-021-04365-8>
- [12] A. Shakeri, C. Adanty, Romosozumab (sclerostin monoclonal antibody) for the treatment of osteoporosis in postmenopausal women: a review, *J. Popul. Ther. Clin. Pharm.* 27 (2020) e25–e31, <https://doi.org/10.15586/jptpc.v27i1.655>
- [13] E.G. Estell, C.J. Rosen, Emerging insights into the comparative effectiveness of anabolic therapies for osteoporosis, *Nat. Rev. Endocrinol.* 17 (2021) 31–46, <https://doi.org/10.1038/s41574-020-00426-5>
- [14] Q. Lyu, Therapeutic potential of nucleic acid aptamers against sclerostin in the treatment of osteoporosis, in *Conference Proceedings. 2017, Hong Kong Baptist University.*
- [15] M. Gisbert-Garzarán, M. Manzano, M. Vallet-Regí, Mesoporous silica nanoparticles for the treatment of complex bone diseases: bone cancer, bone infection and osteoporosis, *Pharmaceutics* 12 (2020) 83, <https://doi.org/10.3390/pharmaceutics12010083>
- [16] Y. Niu, M. Yu, S.B. Hartono, J. Yang, H. Xu, H. Zhang, J. Zhang, J. Zou, A. Dexter, W. Gu, C. Yu, Nanoparticles mimicking viral surface topography for enhanced cellular delivery, *Adv. Mater.* 25 (2013) 6233–6237, <https://doi.org/10.1002/adma.201302737>
- [17] D. Shen, J. Yang, X. Li, L. Zhou, R. Zhang, W. Li, L. Chen, R. Wang, F. Zhang, D. Zhao, Biphasic stratification approach to three-dimensional dendritic biodegradable mesoporous silica nanospheres, *Nano Lett.* 14 (2014) 923–932, <https://doi.org/10.1021/nl404316v>
- [18] D. Wang, S. Miller, M. Sima, P. Kopeckova, J. Kopecek, Synthesis and evaluation of water-soluble polymeric bone-targeted drug delivery systems, *Bioconj. Chem.* 14 (2003) 853–859, <https://doi.org/10.1021/bc034090j>
- [19] M. Mahmoudpour, S. Ding, Z. Lyu, G. Ebrahimi, D. Du, J. Ezzati Nazhad Dolatabadi, M. Torbati, Y. Lin, Aptamer functionalized nanomaterials for biomedical applications: Recent advances and new horizons, *Nano Today* 39 (2021) 101177, <https://doi.org/10.1016/j.nantod.2021.101177>
- [20] O. Bondarenko, M. Mortimer, A. Kahru, N. Feliu, I. Javed, A. Kallinen, S. Lin, T. Xia, Y. Song, T.P. Davis, I. Lynch, W.J. Parak, D.T. Leong, P.C. Ke, C. Chen, Y. Zhao, Nanotoxicology and nanomedicine: The Yin and Yang of nano-bio interactions for the new decade, *Nano Today* 39 (2021) 101184, <https://doi.org/10.1016/j.nantod.2021.101184>
- [21] Y. Wang, B. Zhang, X. Ding, X. Du, Dendritic mesoporous organosilica nanoparticles (DMONs): Chemical composition, structural architecture, and promising applications, *Nano Today* 39 (2021) 101231, <https://doi.org/10.1016/j.nantod.2021.101231>
- [22] K.B. Farrell, A. Karpeisky, D.H. Thamm, S. Zinnen, Bisphosphonate conjugation for bone specific drug targeting, *Bone Rep.* 9 (2018) 47–60, <https://doi.org/10.1016/j.bonr.2018.06.007>
- [23] C. Jing, B. Li, H. Tan, C. Zhang, H. Liang, H. Na, S. Chen, C. Liu, L. Zhao, Alendronate-decorated nanoparticles as bone-targeted alendronate carriers for potential osteoporosis treatment, *ACS Appl. Bio Mater.* 4 (2021) 4907–4916, <https://doi.org/10.1021/acsbm.1c00199>
- [24] L.J. del Valle, O. Bertran, C. Chaves, G. Revilla-López, M. Rivas, M.T. Casas, J. Casanovas, P. Turon, J. Puiggali, C. Alemán, DNA adsorbed on hydroxyapatite surfaces, *J. Mater. Chem. B* 2 (2014) 6953–6966, <https://doi.org/10.1039/C4TB01184H>
- [25] P.K. Suen, L. Qin, Sclerostin, an emerging therapeutic target for treating osteoporosis and osteoporotic fracture: a general review, *J. Orthop. Transl.* 4 (2016) 1–13, <https://doi.org/10.1016/j.jot.2015.08.004>
- [26] Z.H. Zhang, X.Y. Jia, J.Y. Fang, H. Chai, Q. Huang, C. She, P. Jia, D.C. Geng, W. Xu, Reduction of SOST gene promotes bone formation through the Wnt/ β -catenin signalling pathway and compensates particle-induced osteolysis, *J. Cell. Mol. Med.* 24 (2020) 4233–4244, <https://doi.org/10.1111/jcmm.15084>
- [27] P. Korn, I. Kramer, F. Schlottig, N. Tödttman, U. Eckelt, A. Bürki, S.J. Ferguson, A. Kautz, M. Schnabelrauch, U. Range, M. Kneissel, B. Stadlinger, Systemic sclerostin antibody treatment increases osseointegration and biomechanical competence of zoledronic-acid-coated dental implants in a rat osteoporosis model, *Eur. Cell Mater.* 37 (2019) 333–346, <https://doi.org/10.22203/eCM.v037a20>
- [28] Y. Jiang, Y. Li, C. Richard, D. Scherman, Y.S. Liu, Hemocompatibility investigation and improvement of near-infrared persistent luminescent nanoparticle ZnGa₂O₄:Cr³⁺ by surface PEGylation, *J. Mater. Chem. B* 7 (2019) 3796–3803, <https://doi.org/10.1039/c9tb00378a>
- [29] J.H. Zhou, J. Rossi, Aptamers as targeted therapeutics: current potential and challenges, *Nat. Rev. Drug Discov.* 16 (2017) 181–202, <https://doi.org/10.1038/nrd.2016.199>
- [30] Z. Li, Z. Wang, P.C. Dinh, D. Zhu, K.D. Popowski, H. Lutz, S. Hu, M.G. Lewis, A. Cook, H. Andersen, J. Greenhouse, L. Pessaint, L.J. Lobo, K. Cheng, Cell-mimicking nanodecoys neutralize SARS-CoV-2 and mitigate lung injury in a non-human primate model of COVID-19, *Nat. Nanotechnol.* 16 (2021) 942–951, <https://doi.org/10.1038/s41565-021-00923-2>
- [31] X.D. Xie, H.F. Nie, Y. Zhou, S. Lian, H. Mei, Y.S. Lu, H.Y. Dong, F.Q. Li, T. Li, B.F. Li, J. Wang, M. Lin, C.H. Wang, J.W. Shao, Y. Gao, J.M. Chen, F.W. Xie, L. Jia, Eliminating blood oncogenic exosomes into the small intestine with aptamer-functionalized nanoparticles, *Nat. Commun.* 10 (2019) 5476, <https://doi.org/10.1038/s41467-019-13316-w>
- [32] C. Zhang, L. Yan, X. Wang, S. Zhu, C. Chen, Z. Gu, Y. Zhao, Progress, challenges, and future of nanomedicine, *Nano Today* 35 (2020) 101008, <https://doi.org/10.1016/j.nantod.2020.101008>
- [33] Y.-S. Yang, J. Xie, S. Chaugule, D. Wang, J.-M. Kim, J. Kim, P.W.L. Tai, S.-k. Seo, E. Gravalles, G. Gao, J.-H. Shim, Bone-targeting AAV-mediated gene silencing in osteoclasts for osteoporosis therapy, *Mol. Ther. -Meth. Clin. D* 17 (2020) 922–935, <https://doi.org/10.1016/j.omtm.2020.04.010>
- [34] D. Lee, D.N. Heo, H.J. Kim, W.K. Ko, S.J. Lee, M. Heo, J.B. Bang, J.B. Lee, D.S. Hwang, S.H. Do, I.K. Kwon, Inhibition of osteoclast differentiation and bone resorption by bisphosphonate-conjugated gold nanoparticles, *Sci. Rep.* 6 (2016) 27336, <https://doi.org/10.1038/srep27336>
- [35] P. Mora-Raimundo, D. Lozano, M. Benito, F. Mulero, M. Manzano, M. Vallet-Regí, Osteoporosis remission and new bone formation with mesoporous silica nanoparticles, *Adv. Sci.* 8 (2021) e2101107, <https://doi.org/10.1002/advs.202101107>
- [36] Y. Xie, X. Tan, J. Huang, H. Huang, P. Zou, J. Hu, Atorvastatin-loaded micelles with bone-targeted ligand for the treatment of osteoporosis, *Drug Deliv.* 24 (2017) 1067–1076, <https://doi.org/10.1080/10717544.2017.1347966>
- [37] S. Tao, S.-q Chen, W.-t Zhou, F.-y Yu, L. Bao, G.-x Qiu, Q. Qiao, F.-q Hu, J.-w Wang, H. Yuan, A novel biocompatible, simvastatin-loaded, bone-targeting lipid nanocarrier for treating osteoporosis more effectively, *RSC Adv.* 10 (2020) 20445–20459, <https://doi.org/10.1039/d0ra00685h>
- [38] A.G. Benahmed, A. Gasmi, A. Menzel, I. Hrynovets, S. Chirumbolo, M. Shanaida, R. Lysiuk, Y. Shanaida, M. Dadar, G. Bjørklund, A review on natural teeth whitening, *J. Oral. Biosci.* 64 (2021) 49–58, <https://doi.org/10.1016/j.job.2021.12.002>
- [39] K. Strojjan, A. Leonardi, V.B. Bregar, I. Križaj, J. Svete, M. Pavlin, Dispersion of nanoparticles in different media importantly determines the composition of their protein corona, *PLoS One* 12 (2017) e0169552, <https://doi.org/10.1371/journal.pone.0169552>
- [40] I. Kaur, L.-J. Ellis, I. Romer, R. Tantra, M. Carriere, S. Allard, M. Mayne-L'Hermite, C. Minelli, W. Unger, A. Potthoff, S. Rades, E. Valsami-Jones, Dispersion of nanomaterials in aqueous media: towards protocol optimization, *J. Vis. Exp.* (2017) 56074, <https://doi.org/10.3791/56074>
- [41] P. Mora-Raimundo, M. Manzano, M. Vallet-Regí, Nanoparticles for the treatment of osteoporosis, *AIMS Bioeng.* 4 (2017) 259–274, <https://doi.org/10.3934/bioeng.2017.2.259>
- [42] T. Zhao, A. Elzatahry, X. Li, D. Zhao, Single-micelle-directed synthesis of mesoporous materials, *Nat. Rev. Mater.* 4 (2019) 775–791, <https://doi.org/10.1038/s41578-019-0144-x>
- [43] P. Zhang, Y. Li, W. Tang, J. Zhao, L. Jing, K.J. McHugh, Theranostic nanoparticles with disease-specific administration strategies, *Nano Today* 42 (2022) 101335, <https://doi.org/10.1016/j.nantod.2021.101335>
- [44] A. Popat, S. Jambhrunkar, J. Zhang, J. Yang, H. Zhang, A. Meka, C. Yu, Programmable drug release using bioresponsive mesoporous silica nanoparticles for site-specific oral drug delivery, *Chem. Commun.* 50 (2014) 5547–5550, <https://doi.org/10.1039/c4cc00620h>
- [45] K.S. Kim, K. Suzuki, H. Cho, Y.S. Youn, Y.H. Bae, Oral nanoparticles exhibit specific high-efficiency intestinal uptake and lymphatic transport, *ACS Nano* 12 (2018) 8893–8900, <https://doi.org/10.1021/acsnano.8b04315>